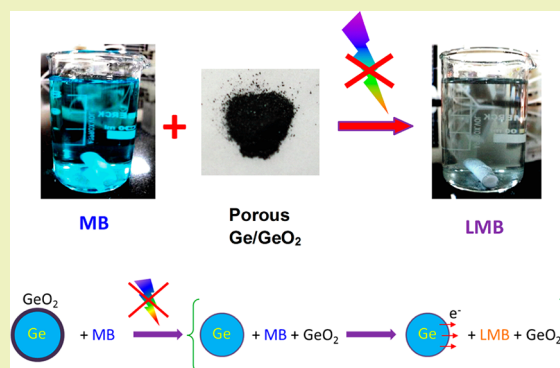


Photon-Free Degradation of Dyes by Ge/GeO<sub>2</sub> Porous MicrostructuresSatish Laxman Shinde<sup>†,‡</sup> and Karuna Kar Nanda<sup>\*,†</sup><sup>†</sup>Materials Research Centre, Indian Institute of Science, Bangalore - 560012, India<sup>‡</sup>International Center for Materials Nanoarchitectonics, National Institute for Materials Science, Tsukuba, Ibaraki 305-0044, Japan

## Supporting Information

**ABSTRACT:** Several industries use dyes as coloring agents and release untreated effluents in the form of wastewater that has created panic due to the environmental issue. Considerable efforts have been extended to develop photocatalysts for the degradation of these dyes. Here, we report the photon-free degradation of various cationic and anionic dyes for the first time by Ge/GeO<sub>2</sub> porous microstructures. The degradation efficiency and time are found to be dependent on the catalyst amount, and it is possible to achieve ~100% degradation without any external stimuli. Our experimental results indicate that Ge donates electrons either directly to dye molecules or to dissolved oxygen (O<sub>2</sub>) molecules and creates superoxide species without any extra energy source that bleaches or degrades the dyes. However, it is essential to have a continuous supply of electrons from Ge to sustain the degradation process.

**KEYWORDS:** Photon-free, Catalysis, Microcrystals, Dyes, Germanium



## INTRODUCTION

Over the past several years, considerable efforts have been expended to develop photocatalysts for the degradation of various dyes with the motive of removing contaminants from wastewater.<sup>1–11</sup> Oxides such as TiO<sub>2</sub>, ZnO, SnO<sub>2</sub>,  $\alpha$ -Fe<sub>2</sub>O<sub>3</sub>, Al<sub>2</sub>O<sub>3</sub>, etc. have been widely explored for this purpose.<sup>12–16</sup> However, practical applications of such materials are limited by their low photocatalytic activity in solar light,<sup>12,17</sup> as these oxides are wide band gap materials. The common strategies for developing visible photocatalysts are doping and the sensitization of wide band gap materials by low band gap ones.<sup>1,18</sup> It may be noted that the semiconducting catalysts can be used not only for the degradation of dyes but also for other organic pollutants such as erythrosine, Eosin Y, phenol, yellow auramine dye, benzene–toluene–xylene (BTX), etc.<sup>5,9</sup> Organic contaminants either degrade into colorless form or dissociate and evaporate in the form of CO<sub>2</sub> by the photocatalysts that generate reactive oxygen species (ROS) including the superoxide radical (O<sub>2</sub><sup>-</sup>), hydroxyl radical (<sup>•</sup>OH), and peroxide (H<sub>2</sub>O<sub>2</sub>).<sup>19–26</sup> Though the decontamination of water is achieved through the latter process, the colorless form of some dyes has various applications. The leuco-methylene blue (LMB) and leuco-malachite green (LMG) are the colorless forms of methylene blue and malachite green, respectively, which can be used in data storage,<sup>27</sup> holographic industries,<sup>28</sup> colorimetric oxygen indicators in food and pharmaceutical industries, etc.<sup>29</sup>

In the case of hybrids, electron exchange takes place that is highly beneficial for catalytic activity. It is reported for Si/SiO<sub>x</sub>

that electrons tunnel from the core through the oxide layer to generate superoxides species for degradation of organic dyes without any external stimuli.<sup>25,30</sup> As the electron concentration of Ge is ~10<sup>3</sup> higher as compared to Si at 300 K, it is expected that Ge@GeO<sub>2</sub> can also be used for the degradation of dyes without any external stimuli and the rate constant is expected to be high. Recently, Ge- and GeO<sub>2</sub>-based materials with unique structures have been extensively studied for various applications.<sup>31–33</sup>

Here, we report the photon-free catalytic activity of Ge/GeO<sub>2</sub> porous microstructures in the degradation of methylene blue (MB), malachite green (MG), congo red (CR), and methyl orange (MO). It is observed that ~100% degradation efficiency can easily be achieved, and the efficiency is optimum at room temperature. When Ge/GeO<sub>2</sub> is used, the degradation of the dyes takes place along with its transformation to Ge with thin oxide core–shell structures whose reusability has been demonstrated. Superoxide generation through the supply of electron from Ge core to the molecular oxygen (O<sub>2</sub>) and direct supply of electrons to the dye molecules mainly help for the photon-free degradation. Overall, Ge/GeO<sub>2</sub> with the large surface area is an efficient catalyst material that shows high stability in degradation of cationic and anionic dyes and is expected to find potential applications for removal of organic waste from water without any external stimuli.

**Received:** October 27, 2018

**Revised:** January 11, 2019

**Published:** February 28, 2019

## RESULTS AND DISCUSSION

Figure S1a,b shows the SEM images of Ge microcrystals before and after annealing. The Ge microcrystals have a size of  $\sim 1\text{--}5\ \mu\text{m}$  and after annealing become aggregate and porous (Figure S1b), having the pore size ranging from 100 nm to  $5\ \mu\text{m}$ . The XRD patterns of Ge microcrystals and Ge/GeO<sub>2</sub> are shown in Figure S1c. The peaks are indexed to the hexagonal  $\alpha$ -quartz phase of GeO<sub>2</sub> (JCPDF No. 43-1016) and the cubic phase of Ge (JCPDF No. 04-0545).<sup>34,35</sup> The Ge microcrystals show only the cubic phase, while the annealed sample confirms the formation of GeO<sub>2</sub> on Ge surface. TEM images also support the Ge/GeO<sub>2</sub> core/shell structure formation (Figure S2). From the HRTEM images, the *d*-spacing is observed to be 0.314 nm for Ge core and 0.335 nm for GeO<sub>2</sub> shell, which is in good agreement with that of the cubic phase of Ge and hexagonal  $\alpha$ -quartz type GeO<sub>2</sub> crystal (JCPDF 04-0545, 43-1016). Both XRD and TEM results corroborate the formation of hexagonal GeO<sub>2</sub> shell on Ge core.

In order to further support the core/shell structure formation of Ge/GeO<sub>2</sub>, we performed the EDS elemental mapping for “Ge” and “O” on the small portion of Ge/GeO<sub>2</sub> microcrystals as shown in Figure S3. It is evident that the core region is mostly of Ge ( $\sim 95\ \text{wt}\ %\ \text{Ge}$  and  $\sim 5\ \text{wt}\ %\ \text{O}$ ) and the outer shell is of GeO<sub>2</sub> ( $\sim 68\ \text{wt}\ %\ \text{Ge}$  and  $\sim 32\ \text{wt}\ %\ \text{O}$ ), confirming the formation of core/shell structure of Ge/GeO<sub>2</sub>. From the SEM images, as shown in Figures S1a,b, S3, and S4, it is observed that the oxidation of Ge is nonuniform and oxide thickness varies at different positions; the average thickness of oxide is measured to be  $\sim 200\ \text{nm}$  (Figure S4). Due to the nonuniform oxidation on Ge, it is difficult to know the exact amount of oxide on Ge and the concentration of Ge and GeO<sub>2</sub> in the hybrid.

The catalytic experiments were carried out using 0.2 g/L Ge/GeO<sub>2</sub> and  $5\ \mu\text{M}$  MB solutions in dark environment with continuous stirring. Figure 1a shows the UV–visible absorption spectra of MB recorded at different reaction time. The strong peak at 663 nm is the characteristic peak of MB<sup>19–21</sup> and decreases, and the new peak appearing at 256 nm corresponds to the LMB (Figure S5) and increases with time.<sup>21</sup> However, little variation in LMB peak intensity may arise due to the various pathways are responsible for MB degradation. Figure 1b shows the relative concentration of MB with time. The reduction follows pseudo-first order reaction rate kinetics

$$-\ln(C/C_0) = kt$$

where  $C_0$  and  $C$  denote the initial concentration and the concentration of dyes at a reaction time  $t$  and  $k$  is the reaction rate constant. The reaction rate constant ( $k$ ) is found to be  $0.077\ \text{min}^{-1}$  which is much higher than the reported values for the other wide band gap materials.<sup>12,19–21,36</sup> It may be noted from Figure 1a that MB reduces by 90% within 30 min. Figure 1c shows the scheme for degradation of MB to LMB. The blue colored MB solution turns to colorless LMB<sup>19,20</sup> after addition of porous Ge/GeO<sub>2</sub>.

The reduction kinetics is studied to probe the effect of Ge/GeO<sub>2</sub> loading (0.2–1.0 g/L) for  $5\ \mu\text{M}$  of MB and that of dye concentration (5–15  $\mu\text{M}$ ) with 0.2 g/L of loading. Figure 1d shows the relative concentration ( $C/C_0$ ) as a function of time for different loadings. When the catalyst loading is increased from 0.2 to 1.0 g/L,  $\sim 100\%$  degradation is achieved at a reaction time of 10 min. Figure 1e shows the variation of

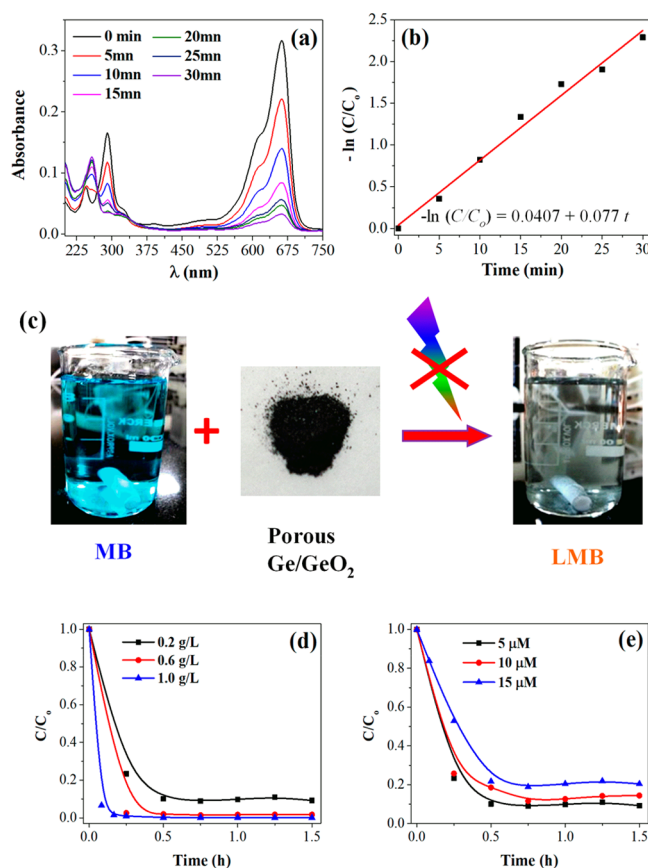


**Figure 1.** Photon-free degradation of MB. (a) UV–visible absorption spectra with time. (b) Relative concentration as a function of time. The data is fitted to a Pseudo-first-order reaction rate equation as shown in an inset. (c) Scheme for the degradation of MB to LMB. Relative concentration as a function of (d) catalyst loading and (e) dye concentration.

relative concentration with time for the different concentrations of MB. As the concentration increases from 5 to 15  $\mu\text{M}$ ,  $\sim 70\%$  degradation is achieved even at a reaction time of 45 min. For higher concentration of dye, the degradation efficiency decreases as the availability of active sites decreases.<sup>12</sup>

We investigate the catalytic activity of Ge microcrystals (commercial) and GeO<sub>2</sub> (prepared by heating Ge microcrystals at 950 °C for 6 h in air ambient)<sup>34</sup> on the degradation of MB as shown in Figure S6. The degradation within 30 min is  $\sim 10\%$  for Ge, less than 1% for GeO<sub>2</sub>, and  $\sim 90\%$  for Ge/GeO<sub>2</sub>. These indicate that Ge/GeO<sub>2</sub> porous microstructures are more efficient in the degradation of MB, while Ge and GeO<sub>2</sub> exhibit very poor catalytic activity. We also investigate the effect of UV/visible light on the degradation of MB by Ge/GeO<sub>2</sub>. Figure S7 shows the variation of relative concentration with time under UV light ( $\lambda = 265\ \text{nm}$ ) for  $5\ \mu\text{M}$  MB and 0.2 g/L Ge/GeO<sub>2</sub>. The comparison of the results (Figures 1d and S7) obtained without and with UV light indicates that light has no/minimal effect on the degradation process. The as-prepared Ge/GeO<sub>2</sub> sample has various interfacial and oxygen vacancies defects.<sup>34,35</sup> The photoexcited electron–hole pairs might be recombined at the Ge/GeO<sub>2</sub> interface due to the high density of defect,<sup>34,35</sup> resulting in nearly equal degradation rate with and without UV light.

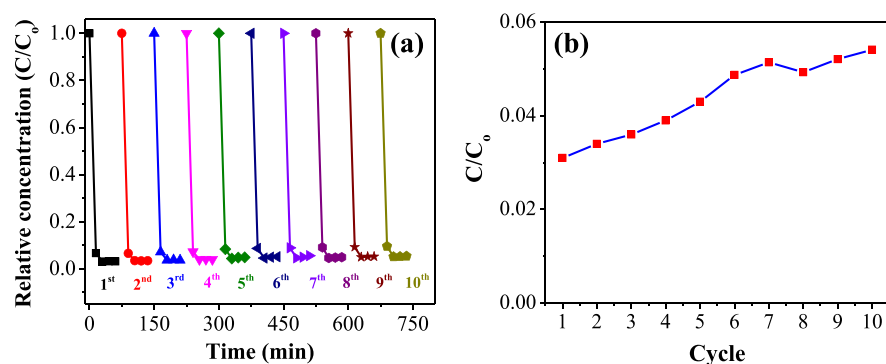


**Figure 2.** (a) Catalytic stability of the Ge/GeO<sub>2</sub> for degradation of MB for 10 cycling runs. (b) Relative concentration of degradation of MB after 30 min for each cycle.

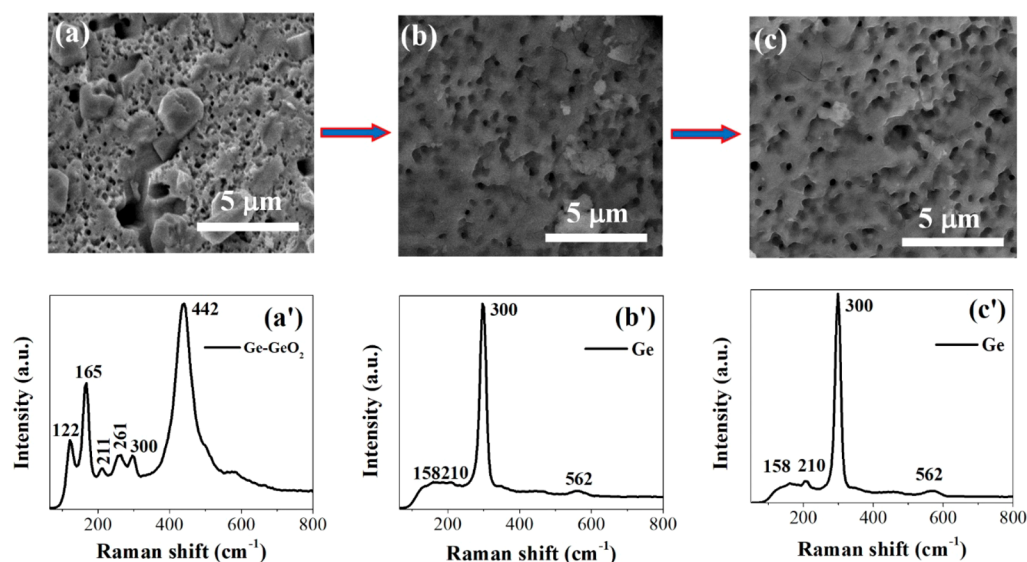


**Figure 3.** SEM images and Raman spectra of (a and a') as-prepared catalyst and used catalyst after the (b and b') 1st cycle and the (c and c') 5th cycle.

The reusability was examined for 10 consecutive cycles as shown in Figure 2a. Here, 0.5 g/L catalyst is used to convert 5  $\mu\text{M}$  MB. Figure 2b shows the relative concentration of degradation of MB within 30 min. The results indicate that the percentage of degradation decreases gradually which may be due to the loss of material during the recovery of materials after each cycle.

To shed light on the degradation phenomena for MB, we investigate the morphology as well as the structures of as-synthesized and used Ge/GeO<sub>2</sub>. Surprisingly, after the first cycle, GeO<sub>2</sub> desorbs from Ge/GeO<sub>2</sub> and reduces to Ge as observed in Raman spectra (Figure 3a',b') along with a change in porosity (Figure 3a,b). The Raman peaks at 122, 165, 211, and 261  $\text{cm}^{-1}$  and a strong peak at 442  $\text{cm}^{-1}$  are indicative of the trigonal phase of GeO<sub>2</sub>, while the weak peak at 300  $\text{cm}^{-1}$  is due to Ge.<sup>28</sup> However, a strong peak at 300  $\text{cm}^{-1}$  is observed for used catalyst indicating the conversion of Ge/GeO<sub>2</sub> into Ge (Figure 3b').<sup>28,29</sup> Figure 3c,c' shows the SEM image and Raman spectrum of the catalyst obtained after the fifth cycle. The porous morphology (Figure 3c) and the strong peak at 300  $\text{cm}^{-1}$  (Figure 3c') are observed as is the case of Figure 3b,b'. No signature of GeO<sub>2</sub> is observed in Raman spectra of used catalyst, due to the very thin layer of GeO<sub>2</sub> on Ge surface as evident from the XPS results.

For detailed investigation on the phase of the catalyst, we perform EDS and XPS analysis. The EDS spectra (Figure S8) show that the Ge:O atomic ratios (Table S1) are 37:61 and 45:40 for as-prepared and used catalyst, respectively. This indicates the formation of an oxide layer on the surface after use. This is further confirmed by XPS analysis. The deconvoluted XPS spectra for Ge 3d (Figure S9a) and O 1s (Figure S9b) core-level electrons of as-prepared Ge/GeO<sub>2</sub> confirm the major phase of GeO<sub>2</sub> along with weak signature of Ge, GeO<sub>x $\approx$ 1</sub>, and GeO<sub>x $\approx$ 2</sub> phases.<sup>37</sup> For the used catalyst obtained after 5 cycles (Figure S9c,d), the major phase was observed to be GeO<sub>2</sub> and GeO<sub>x $\approx$ 2</sub> along with weak peaks of Ge and GeO<sub>x $\approx$ 1</sub> phases.<sup>37</sup> XPS analysis reveals that the phase of catalyst (Ge/GeO<sub>2</sub>) during catalysis reaction changes to Ge/GeO<sub>x $\approx$ 2</sub> with oxygen vacancies and ascertains the presence of the oxide layer on Ge. The cation states of Ge are observed to be Ge<sup>2+</sup> and Ge<sup>4+</sup>. The BET surface area for the porous Ge/GeO<sub>2</sub> before and after catalysis (5 cycles) is found to be 15.75 and 16.11  $\text{m}^2/\text{g}$  (Figure S10), respectively suggesting a small improvement in the porosity. Overall, Ge with thin oxide porous structures is essential for the degradation of dyes, as bulk Ge and GeO<sub>2</sub> shows very weak catalytic activity (Figure S6). Apparently, Ge/GeO<sub>2</sub> is a well-reproducible catalyst and can be used as effective photon-free catalysts for degradation of

dyes. The morphology (Figure 3b,c) and activity (Figure 2) of Ge/GeO<sub>2</sub> show negligible variation with reuse.

It is well-known that the chemical reaction rate increases with increase in temperature and vice versa. To study the effect of temperature on degradation of dyes, the catalytic experiments are performed in a temperature range of 10 to 45 °C for 5 μM MB solutions with the addition of 0.2 g/L Ge/GeO<sub>2</sub>. It is interesting to note that the degradation rate is optimum around room temperature (Figure S11). The degradation within 30 min is 90% at 25 °C, while it is 20 and 45% at 10 and 45 °C, respectively. The degradation is expected to be slow at low temperature. Surprisingly, the degradation is slow at high temperature as well. It may be noted from Figure S11 that the absorbance initially decreases and then increases at 45 °C, and this indicates the conversion of LMB into MB. Temperature hinders the degradation process and increases the oxidation of LMB; as a consequence, the overall reaction is slow.

The scheme for degradation reaction of MB is shown in Figure 4a. MB reduces to LMB by accepting the electrons.<sup>21</sup> Based on experimental observation, a scheme for the degradation mechanism has been presented (Figure 4b). When Ge/GeO<sub>2</sub> is added to MB solution, some amount of GeO<sub>2</sub> desorbs into solution, and we are left with Ge with the thin oxide layer.<sup>38</sup> It is reported for Si/SiO<sub>x</sub> as well as for Fe@Fe<sub>2</sub>O<sub>3</sub> core-shell nanowires, that electron transfer/tunnel through the oxide layer to molecular O<sub>2</sub> present in water, which results in the formation of reactive oxygen species such as superoxides O<sub>2</sub><sup>•-</sup>, HO<sub>2</sub><sup>•</sup>, etc.<sup>25,30</sup> These superoxide species are highly reactive and degrades the various dyes.<sup>25,30</sup> Similarly, for the case of Ge with the thin oxide layer of GeO<sub>2</sub>, the electron transfer process is spontaneous, as the work function of Ge (~4.04 eV) is lower than that of GeO<sub>2</sub> (~4.9 eV).<sup>39,40</sup> Therefore, electrons will flow from the Ge core to the conduction band of the GeO<sub>2</sub> shell until the position of their Fermi energy levels are adjusted to the same level.<sup>39,40</sup>

The whole degradation process began with donating electron from Ge core without external stimuli. The degradation mechanism can have two pathways: (i) indirect participation of electrons by creating radicals or (ii) direct transfer of electrons to dye molecules. Energy band diagram of Ge/GeO<sub>2</sub> and standard redox potentials ( $E_0$ ) with respect to vacuum energy level and normal hydrogen electrode (NHE) scale of different reactive species are shown in Figure 4c.

The electron transfer from Ge core can react with the dissolved O<sub>2</sub> to form the superoxides radical (O<sub>2</sub><sup>•-</sup>) as the redox potential of Ge ( $E_0 = -4.0$  eV) is more negative than that of the O<sub>2</sub>/O<sub>2</sub><sup>•-</sup> ( $E_0 = -4.34$  eV).<sup>41</sup> Further, superoxide radical (O<sub>2</sub><sup>•-</sup>) can undergo protonation to produce hydroxyl radicals (<sup>•</sup>OH).<sup>41</sup> To maintain a constant flow of electrons from Ge core to the dye/O<sub>2</sub> molecules, a continuous supply of electrons is required. The electrons may come from the oxidation of Ge. This suggests that the degradation process is accompanied by the thickening and simultaneous desolution of the GeO<sub>2</sub> shell into solution, thereby maintaining the thin oxide layer on the Ge surface and degradation rate. Formation of other oxidative species such as HO<sub>2</sub><sup>•</sup> and OH<sup>-</sup> from O<sub>2</sub> is also favorable since corresponding redox potentials (O<sub>2</sub>/HO<sub>2</sub><sup>•</sup> = -4.65 eV and O<sub>2</sub>/OH<sup>-</sup> = -4.8 eV) lie below the conduction band of Ge (Figure 4c).<sup>42</sup> Similarly, direct electron transfer from Ge/GeO<sub>2</sub> to MB and formation of semireduced MB (MB<sup>•-</sup>) and LMB is also possible as the  $E_0$  of MB/MB<sup>•-</sup> (-4.27 eV) and MB/LMB (-4.51 eV) are lower than the CB of Ge (Figure 4c).<sup>41,42</sup> Considering the large difference in

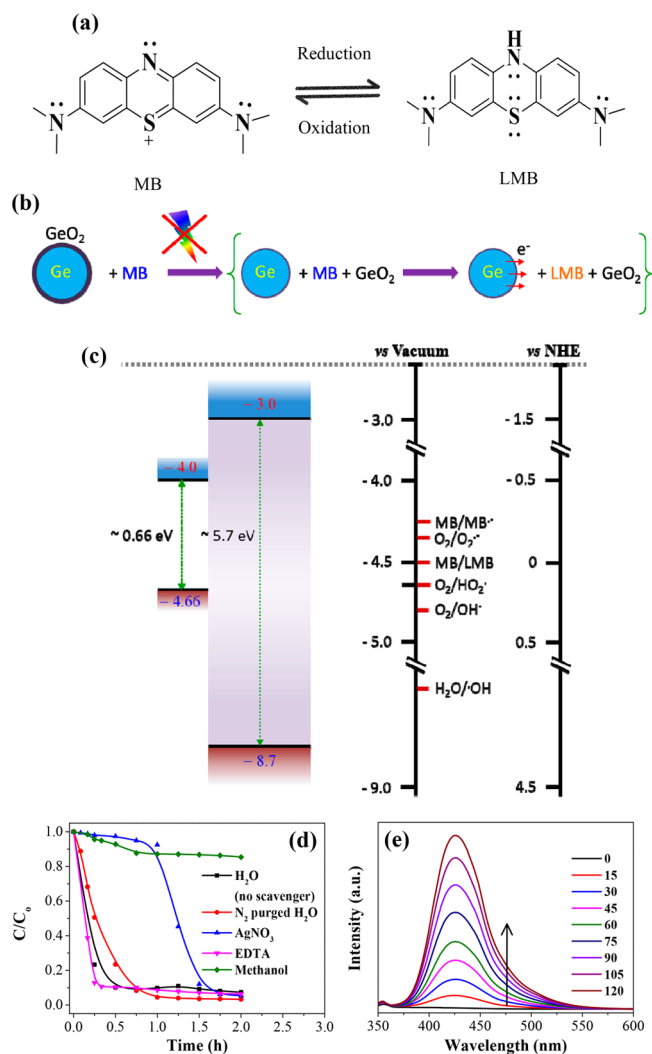


**Figure 4.** (a) Structures and (b) mechanism for the conversion of MB to LMB. (c) Energy level diagram of Ge/GeO<sub>2</sub> and standard redox potential ( $E_0$ ) of different oxidative species with respect to vacuum energy levels and the normal hydrogen electrode (NHE). (d) Effect of radical scavenger/quencher on the degradation process of 0.5 μM MB with the addition of 0.2 g/L Ge/GeO<sub>2</sub>. (e) PL spectrum of terephthalic acid at regular time (min) intervals to detect <sup>•</sup>OH radicals generated during the catalysis process. The excitation wavelength is 315 nm.

redox potential of H<sub>2</sub>O/<sup>•</sup>OH (-6.82 eV) and valence band of Ge (-4.66 eV), the direct oxidation of H<sub>2</sub>O by holes is not favorable (Figure 4c).<sup>43,44</sup>

To confirm the dissolution of GeO<sub>2</sub> into the solution during catalysis, Ge/GeO<sub>2</sub> microcrystals are allowed to settle in the solution for 24 h. The clear solution is then removed and dried on the glass plate to check the presence of GeO<sub>2</sub> using Raman spectroscopy. The Raman spectrum that is shown in Figure S12a reveals a strong peak at 444 cm<sup>-1</sup> corresponding to the GeO<sub>2</sub> phase that confirms the presence of dissolved GeO<sub>2</sub> in the solution. To check any influence of dissolved GeO<sub>2</sub> on dye degradation, we added the MB dye into the GeO<sub>2</sub> containing the solution. Raman spectra as shown in Figure S12b clearly reveal that dissolved GeO<sub>2</sub> does not participate in the dye degradation.

To further support the reaction mechanism, the effect of different radical scavengers on the degradation process of MB

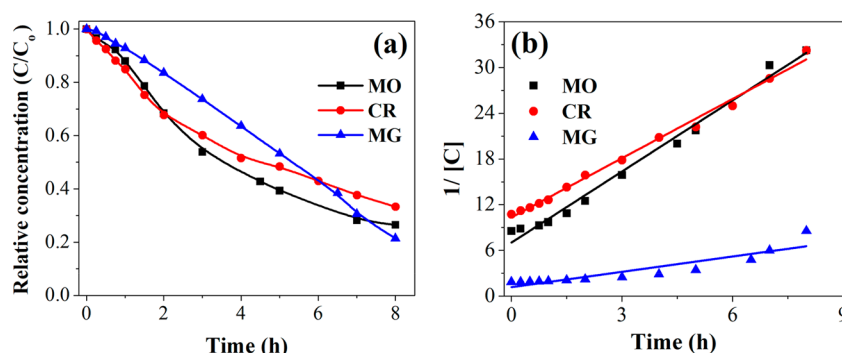


**Figure 5.** (a) Relative concentration as a function of time for MO, CR, and MG. (b) Pseudo-second order fit for MO, CR, and MG, respectively.

are studied. Interestingly, use of silver nitrate as electron scavenger decreases the MB degradation rate significantly in comparison to H<sub>2</sub>O with no scavenger followed by an enhancement in degradation rate.<sup>45,46</sup> This suggests that, initially, AgNO<sub>3</sub> prevents the reaction of electrons with dye/O<sub>2</sub> molecules. With time AgNO<sub>3</sub> becomes saturated and increases the degradation rate, as electron transfer from Ge is a continuous process. This also supports that during catalysis reaction simultaneous formation and desorption of GeO<sub>2</sub> on the Ge surface and leads to the continuous supply of electrons. However, an addition of hole scavengers (Na<sub>2</sub>-EDTA) has no influence on the MB degradation rate (Figure 4d) due to the large difference in redox potential between H<sub>2</sub>O/•OH and the valence band of Ge (Figure 4c).<sup>43–46</sup> When methanol (•OH radical scavengers) is used as a solvent, the degradation rate is found to be reduced since the formation of •OH radicals is prevented (Figure 4d).<sup>45,46</sup> To perform MB degradation in an oxygen-free atmosphere, N<sub>2</sub> was purged for 2 h in H<sub>2</sub>O. Initially, the reaction rate of MB degradation slightly decreases compared to air-equilibrated conditions, which again increases with time (Figure 4d). In the absence of dissolved O<sub>2</sub>, electrons react with H<sub>2</sub>O, which generates •OH radicals for the degradation of dyes. In the presence of dissolved O<sub>2</sub>, the reaction rate is higher indicating the role of dissolved oxygen in the degradation of dyes. With longer (more than 2 days) exposure to air, the MB<sup>•−</sup>/LMB can reversibly convert into MB.<sup>21</sup> These results indicate that the direct transfer of conduction band electrons of Ge to MB and H<sub>2</sub>O/dissolved O<sub>2</sub> to form superoxides species, which generates •OH radicals. These are the possible reaction pathways believed to be involved in the degradation process of MB. We used terephthalic acid as a probe molecule to detect the •OH radicals formation during catalysis reaction. The •OH radicals react with the terephthalic acid and produce fluorescent 2-hydroxyterephthalic acid (TAOH).<sup>47</sup> After addition of 0.2 g/L Ge/GeO<sub>2</sub> in 5 mM solution of terephthalic acid, the PL intensity increases with time as shown in Figure 4e. This confirms the gradual formation of •OH radicals during catalysis reaction in the presence of Ge/GeO<sub>2</sub>. These highly reactive hydroxyl radicals further degrade the LMB into carbon dioxide (CO<sub>2</sub>) and water.<sup>21</sup>

Compared to Ge/GeO<sub>2</sub>, pure Ge shows very low degradation rate in the beginning (Figure S6d) which increases with time as the GeO<sub>2</sub> oxide forms on the Ge surface during the reaction. This indicates that GeO<sub>2</sub> plays a key role for high degradation rate. The GeO<sub>2</sub> shell possesses various properties like high surface area due to the porous surface and strong affinity to adsorb dye/O<sub>2</sub> molecules.<sup>18</sup> Due to the thin layer of

GeO<sub>2</sub>, wide band gap, and without or with very fewer defects, it prevents the interfacial charge recombination between Ge and dye/O<sub>2</sub> molecules that make Ge/GeO<sub>2</sub> the more efficient catalyst compared to pure Ge. If the oxide layer is thick, the charge transfer is prevented that reduces the catalytic activity and is very poor for GeO<sub>2</sub>. Overall, the optimization of the shell thickness is key for high degradation rate.

We have also studied the degradation of other cationic (MG) and anionic dyes (CR and MO). Figure 5a shows the variation of relative concentration with time for 5 μM of MO, CR, and MG dyes with 0.2 g/L of the catalyst. The percentages of degradation in 8 h are 74, 67, and 79% for MO, CR, and MG, respectively. The degradation of these dyes follows the pseudo-second order rate kinetics (1/C = 1/C<sub>0</sub> + kt) as shown in Figure 5b. The rate constant (*k*) is found to be 0.051, 0.043, and 0.011 min<sup>−1</sup> for MO, CR, and MG dyes, respectively, suggesting slow degradation as compared to MB. Figure S13a,b shows the optical images of color and discoloration of MO before and after degradation. It is also observed that the degradation of MO is almost independent of temperature (Figure S14) but can be enhanced by increasing the catalyst amount.

The degradation mechanism for these dyes is similar to that of MB. All these dyes degrade by both superoxide species and directly accepting electrons from Ge/GeO<sub>2</sub>. The C=C bonds of MG break to form two dissociated molecules which are colorless in nature.<sup>22–24,48,49</sup> For the azo-dyes such as MO and CR, the azo bonds (N=N) are very active, and it can easily be cleaved by reduction.<sup>22–24</sup> The color of azo dyes depends on the N=N bonds, chromophores, etc., and its cleavage gives discoloration as the dye dissociates into smaller molecules.<sup>22–24</sup> The cleavage of the azo bonds results into small organic molecules and, hence, to permanent degradation (Figure S15). The Raman spectra recorded for the used catalyst after degradation of MG and MO (Figure S16) show strong peaks at 300 cm<sup>−1</sup>, respectively, which is a characteristic peak of Ge phase.<sup>36</sup>

The total organic carbon (TOC) present in 5 μM MB before and after degradation is provided in Table S2. TOC before and after 15 min of the degradation is 1.82 and 1.24 mg/L, respectively. This indicates that ~32% removal of organic carbon in the form of CO<sub>2</sub>, and a part of MB gets converted to LMB. However, dyes degrade more than 80% in the form of CO<sub>2</sub> in ~60 min. The percentages of TOC (Table S2) removal for MO, CR, and MG (0.2 g/L Ge/GeO<sub>2</sub> in 4 h) are ~45, ~42, and ~53%, respectively. The hydroxyl radical is mainly responsible for degradation of these dyes. The Ge/GeO<sub>2</sub> catalyst is highly efficient, as it completely degrades the dyes

(MB) in 60 min under dark condition, which is comparable to the state-of-art photocatalyst reported in the literature (Table S3). It is noted that the colorless form of MB (i.e., LMB) and other dyes has various applications. They are also nontoxic to the biological system and can easily be removed by simple oxidation/reduction reactions.<sup>50–52</sup> Ge/GeO<sub>2</sub> can generate superoxide radicals in water spontaneously and does not require light. This is a promising new method for the generation of superoxides; therefore, its application could be expanded from dye degradation into many other research fields where superoxides are involved.

## CONCLUSIONS

In summary, we have demonstrated for the first time a photon-free degradation of cationic (MB, MG) and anionic dyes (CR, MO) by Ge/GeO<sub>2</sub> porous microcrystals with a degradation efficiency of ~100%. Our experimental results indicate that Ge/GeO<sub>2</sub> reduces the dyes by donating electrons from the Ge core directly to the dye molecules or by creating superoxide and hydroxyl radicals without any extra energy source. Overall, due to photon-free, efficient, and well-reproducible catalytic performance, porous Ge/GeO<sub>2</sub> can be considered as a promising candidate for commercial adoptions and motivate researchers to develop other materials for photon-free degradation of different contaminants.

## METHODS

**Chemicals.** Ge microcrystals (Sigma-Aldrich, 99.999% purity), Methylene blue, Malachite green, Congo red, Methyl orange dyes (powder form from Alpha Aesar), silver nitrate (AgNO<sub>3</sub>), disodium-ethylenediaminetetraacetic acid (Na<sub>2</sub>-EDTA), terephthalic acid (C<sub>6</sub>H<sub>4</sub>(COOH)<sub>2</sub>), and methanol (99.8%), from Wako Pure Chemical Industries, Ltd., are used.

**Synthesis of Ge/GeO<sub>2</sub> Microcrystals.** Ge microcrystals are taken in a quartz boat, placed at the center in a horizontal tube furnace (Figure S17), and heated at 600 °C for 6 h. Ge/GeO<sub>2</sub> microstructures are formed when Ge microcrystals are heated in air ambient in a tube closed at both the ends, i.e., in oxygen deficient condition. The sample is collected from a quartz boat that contains only Ge/GeO<sub>2</sub> phase. We did not observe any other phases of Ge (GeO, GeO<sub>2</sub>, etc.) formation at the other sites of the tube.

**Characterization.** The morphology and phase of Ge/GeO<sub>2</sub> microstructures are studied by scanning electron microscopy (SEM) and energy dispersive X-ray spectrometry analysis (EDS) using Quanta 200, high resolution transmission electron microscope (TEM/HRTEM) images using the JEOL JEM-2100F system, Raman spectroscopy with a 532 nm wavelength Nd:YAG laser using WITec system, X-ray diffraction (XRD) with a Panalytical X'Pert Pro diffractometer, and X-ray photoelectron spectroscopy (XPS) by Theta Probe, Thermo Fisher Scientific, Inc. The UV–visible absorption spectra are recorded by a HITACHI U2900 spectrophotometer. Brunauer–Emmett–Teller (BET) surface area is measured by Quantachrome, Autosorb-iQ. The TOC measurements are done by Hach BioTector B3500C TOC analyzer. The photoluminescence (PL) measurements are carried out by a JASCO, FP8500 fluorescence spectrometer.

**Catalytic Reactions.** The catalytic experiments were performed for different concentrations (5–15 μM) of the dyes with different loadings (0.2–1.0 g/L) of Ge/GeO<sub>2</sub>. The catalysis experiments are carried out in the closed box, i.e., in dark environment. The REMI 2MLH magnetic stirrer is used for stirring the solutions. The stirring speed was kept constant at 200 rpm for all experiments. The absorption spectra was measured by taking out 3 mL of solution with the regular time interval. For the reusability test, the catalyst was allowed to settle for 15 min, separated, and rinsed with DI water several times and used for the next cycles. For the detection of radical

scavenger effect, we used 0.2 g/L Ge/GeO<sub>2</sub> in 5 μM MB in the various solvents such as methanol (99.8%), N<sub>2</sub> purged (2 h) H<sub>2</sub>O, 5 mM AgNO<sub>3</sub>, and 5 mM Na<sub>2</sub>-EDTA. For the detection of •OH radicals, we used 0.2 g/L Ge/GeO<sub>2</sub> in an aqueous solution of 0.5 mM terephthalic acid in 2 mM NaOH and stirred. In a regular time interval, 1 mL of solution was taken out, and the PL intensity was analyzed at an excitation wavelength of 315 nm.

## ASSOCIATED CONTENT

### Supporting Information

The Supporting Information is available free of charge on the ACS Publications website at DOI: 10.1021/acssuschemeng.8b05549.

SEM and XRD pattern of Ge/GeO<sub>2</sub>; TEM/HRTEM images of region of Ge/GeO<sub>2</sub> microcrystals; EDS of Ge/GeO<sub>2</sub>; SEM of Ge/GeO<sub>2</sub>; absorption of MB; effect of catalyst on degradation; degradation in UV light; EDS of catalyst; XPS of catalyst; BET surface area of catalyst; effect of temperature on degradation of MB; Raman and absorbance of GeO<sub>2</sub>; optical images of MO degradation; effect of temperature on degradation of MO; schematic of chemical structures of dyes; Raman spectra of Ge after degradation; schematic setup for synthesis; EDS of catalyst (Table S1); and TOC of dyes (Table S2); comparison of catalytic/photocatalytic dye degradation by state-of-art catalyst (Table S3) (PDF)

## AUTHOR INFORMATION

### Corresponding Author

\*E-mail: nanda@iisc.ac.in (K. K. Nanda).

### ORCID

Satish Laxman Shinde: 0000-0002-0353-3705

Karuna Kar Nanda: 0000-0001-9496-1408

### Notes

The authors declare no competing financial interest.

## ACKNOWLEDGMENTS

The authors acknowledge the financial support from Department of Science and Technology (DST) through Nano-mission. The authors also acknowledge Dr. B. K. Barman, Dr. H. K. Sadhanala, Asst. Prof. S. Shanmugamraju, and Dr. A. Dalui for helpful discussion.

## REFERENCES

- (1) Chen, C.; Li, P.; Wang, G.; Yu, Y.; Duan, F.; Chen, C.; Song, W.; Qin, Y.; Knez, M. Nanoporous nitrogen doped titanium dioxide with excellent photocatalytic activity under visible light irradiation produced by molecular layer deposition. *Angew. Chem., Int. Ed.* **2013**, *52*, 9196–9200.
- (2) Asahi, R.; Morikawa, T.; Ohwaki, T.; Aoki, K.; Taga, Y. Visible-light photocatalysis in nitrogen-doped titanium oxides. *Science* **2001**, *293*, 269–271.
- (3) Li, H.; He, X.; Kang, Z.; Huang, H.; Liu, Y.; Liu, J.; Lian, S.; Tsang, C. H. A.; Yang, X.; Lee, S.-T. Water soluble fluorescent carbon quantum dots and photocatalyst design. *Angew. Chem., Int. Ed.* **2010**, *49*, 4430–4434.
- (4) Wang, M.; Iocozzia, J.; Sun, L.; Lin, C.; Lin, Z. Inorganic-modified semiconductor TiO<sub>2</sub> nanotube arrays for photocatalysis. *Energy Environ. Sci.* **2014**, *7*, 2182–2202.
- (5) Siddiq, A.; Sabir, S.; Hussain, S. T.; Muhammad, B. Highly active mesoporous SiO<sub>2</sub>-TiO<sub>2</sub> based nanocomposites for photocatalytic degradation of textile dyes and phenol. *Eur. J. Chem.* **2013**, *4*, 388–395.

- (6) Lettmann, C.; Hinrichs, H.; Maier, W. F. Combinatorial discovery of new photocatalysts for water purification with visible light. *Angew. Chem., Int. Ed.* **2001**, *40*, 3160–3164.
- (7) Basu, M.; Garg, N.; Ganguli, A. K. A Type-II semiconductor (ZnO/CuS heterostructure) for visible light photocatalysis. *J. Mater. Chem. A* **2014**, *2*, 7517–7525.
- (8) Wang, P.; Huang, B.; Qin, X.; Zhang, X.; Dai, Y.; Wei, J.; Whangbo, M. H. Ag@AgCl: A highly efficient and stable photocatalyst active under visible light. *Angew. Chem., Int. Ed.* **2008**, *47*, 7931–7933.
- (9) Pereira, L.; Pereira, R.; Oliveira, C. S.; Apostol, L.; Gavrilescu, M.; Pons, M.-N.; Zahraa, O.; Madalena Alves, M. UV/TiO<sub>2</sub> photocatalytic degradation of xanthene dyes. *Photochem. Photobiol.* **2013**, *89*, 33–39.
- (10) Borgarello, E.; Kiwi, J.; Graetzel, M.; Pelizzetti, E.; Visca, M. Visible light induced water cleavage in colloidal solutions of chromium-doped titanium dioxide particles. *J. Am. Chem. Soc.* **1982**, *104*, 2996–3002.
- (11) Zou, Z.; Ye, J.; Sayama, K.; Arakawa, H. Direct splitting of water under visible light irradiation with an oxide semiconductor photocatalyst. *Nature* **2001**, *414*, 625–627.
- (12) Pande, S.; Ghosh, S. K.; Nath, S.; Praharaj, S.; Jana, S.; Panigrahi, S.; Basu, S.; Pal, T. Reduction of methylene blue by thiocyanate: kinetic and thermodynamic aspects. *J. Colloid Interface Sci.* **2006**, *299*, 421–427.
- (13) Ge, M.; Cao, C.; Huang, J.; Li, S.; Chen, Z.; Zhang, K.-Q.; Al-Deyab, S. S.; Lai, Y. A Review of one-dimensional TiO<sub>2</sub> nanostructured materials for environmental and energy applications. *J. Mater. Chem. A* **2016**, *4*, 6772–6801.
- (14) Hwang, D. W.; Kim, J.; Park, T. J.; Lee, J. S. Mg-doped WO<sub>3</sub> as a novel photocatalyst for visible light-induced water splitting. *Catal. Lett.* **2002**, *80*, 53–57.
- (15) Bousslama, M.; Amamra, M. C.; Jia, Z.; Ben Amar, M.; Chhor, K.; Brinza, O.; Abderrabba, M.; Vignes, J.-L.; Kanaev, A. Nanoparticulate TiO<sub>2</sub>-Al<sub>2</sub>O<sub>3</sub> photocatalytic media: effect of particle size and polymorphism on photocatalytic activity. *ACS Catal.* **2012**, *2*, 1884–1892.
- (16) Al-Hassan, L. A.; Al-Amro, F. S. Photolytic and photosensitized reactions of methylene blue with some cyclic ketones. *J. Photochem. Photobiol., A* **1998**, *112*, 165–171.
- (17) Yoon, T. P.; Ischay, M. A.; Du, J. Visible light photocatalysis as a greener approach to photochemical synthesis. *Nat. Chem.* **2010**, *2*, 527–532.
- (18) Wang, J.; He, Y.; Tao, J.; He, J.; Zhang, W.; Niu, S.; Yan, Z. Enhanced photodegradation of dyes on titania-based photocatalysts by adding commercial GeO<sub>2</sub> in aqueous suspension. *Chem. Commun.* **2010**, *46*, 5250–5252.
- (19) Galagan, Y.; Su, W.-F. Reversible photoreduction of methylene blue in acrylate media containing benzyl dimethyl ketal. *J. Photochem. Photobiol., A* **2008**, *195*, 378–383.
- (20) Sohrabnezhad, Sh. Study of catalytic reduction and photodegradation of methylene blue by heterogeneous catalyst. *Spectrochim. Acta, Part A* **2011**, *81*, 228–235.
- (21) Impert, O.; Katafias, A.; Kita, P.; Mills, A.; Pietkiewicz-Graczyk, A.; Wrzeszcz, G. Kinetics and mechanism of a fast leuco-methylene blue oxidation by copper(II)-halide species in acidic aqueous media. *Dalton Trans.* **2003**, 348–353.
- (22) Houas, A.; Lachheb, H.; Ksibi, M.; Elaloui, E.; Guillard, C.; Herrmann, J.-M. Photocatalytic degradation pathway of methylene blue in water. *Appl. Catal., B* **2001**, *31*, 145–157.
- (23) Lachheb, H.; Puzenat, E.; Houas, A.; Ksibi, M.; Elaloui, E.; Guillard, C.; Herrmann, J.-M. Photocatalytic degradation of various types of dyes (alizarin s, crocein orange g, methyl red, congo red, methylene blue) in water by uv-irradiated titania. *Appl. Catal., B* **2002**, *39*, 75–90.
- (24) Akpan, U. G.; Hameed, B. H. Parameters affecting the photocatalytic degradation of dyes using TiO<sub>2</sub>-based photocatalysts: a review. *J. Hazard. Mater.* **2009**, *170*, 520–529.
- (25) Cao, Y.; Gu, X.; Yu, H.; Zeng, W.; Liu, X.; Jiang, S.; Li, Y. Degradation of organic dyes by Si/SiO<sub>x</sub> core-shell nanowires: spontaneous generation of superoxides without light irradiation. *Chemosphere* **2016**, *144*, 836–841.
- (26) Epling, G. A.; Lin, C. Photoassisted bleaching of dyes utilizing TiO<sub>2</sub> and visible light. *Chemosphere* **2002**, *46*, 561–570.
- (27) Mills, A. Oxygen indicators and intelligent inks for packaging food. *Chem. Soc. Rev.* **2005**, *34*, 1003–1011.
- (28) Ushamani, M.; Sreekumar, K.; Kartha, C. S.; Joseph, R. Complex methylene-blue-sensitized polyvinyl chloride: a polymer matrix for hologram recording. *Appl. Opt.* **2002**, *41*, 1984–1988.
- (29) Ushamani, M.; Sreekumar, K.; Kartha, C. S.; Joseph, R. Fabrication and characterization of methylene-blue-doped polyvinyl alcohol-polyacrylic acid blend for holographic recording. *Appl. Opt.* **2004**, *43*, 3697–3703.
- (30) Ai, Z.; Gao, Z.; Zhang, L.; He, W.; Yin, J. J. Core-shell structure dependent reactivity of Fe@Fe<sub>2</sub>O<sub>3</sub> nanowires on aerobic degradation of 4-chlorophenol. *Environ. Sci. Technol.* **2013**, *47*, 5344–5352.
- (31) Li, D.; Wang, H.; Liu, H. K.; Guo, Z. A new strategy for achieving a high performance anode for lithium ion batteries—encapsulating germanium nanoparticles in carbon nanoboxes. *Adv. Energy Mater.* **2016**, *6*, 1501666.
- (32) Li, D.; Wang, H.; Zhou, T.; Zhang, W.; Liu, H. K.; Guo, Z. Unique structural design and strategies for germanium based anode materials toward enhanced lithium storage. *Adv. Energy Mater.* **2017**, *7*, 1700488.
- (33) Wu, S.; Han, C.; Iocozzia, J.; Lu, M.; Ge, R.; Xu, R.; Lin, Z. Germanium-based nanomaterials for rechargeable batteries. *Angew. Chem., Int. Ed.* **2016**, *55*, 7898–7922.
- (34) Shinde, S. L.; Nanda, K. K. Thermal oxidation strategy for the synthesis of phase-controlled GeO<sub>2</sub> and photoluminescence characterization. *CrystEngComm* **2013**, *15*, 1043–1046.
- (35) Shinde, S. L.; Nanda, K. K. Towards the understanding of formation of micro/nano holes of Ge/GeO<sub>2</sub> through phase mapping. *CrystEngComm* **2013**, *15*, 4049–4053.
- (36) Atuchin, V. V.; Gavrilova, T. A.; Gromilov, S. A.; Kostrovsky, V. G.; Pokrovsky, L. D.; Troitskaia, I. B.; Vemuri, R. S.; Carbajal-Franco, G.; Ramana, C. V. Low-temperature chemical synthesis and microstructure analysis of GeO<sub>2</sub> crystals with  $\alpha$ -quartz structure. *Cryst. Growth Des.* **2009**, *9*, 1829–1832.
- (37) Prabhakaran, K.; Ogino, T. Oxidation of Ge(100) and Ge(111) surfaces: An UPS and XPS study. *Surf. Sci.* **1995**, *325*, 263–271.
- (38) Wang, C.; Tang, P.; Ge, M.; Xu, X.; Cao, F.; Jiang, J. Z. Synthesis and characterization of gold cubic nanoshells using water-soluble GeO<sub>2</sub> templates. *Nanotechnology* **2011**, *22*, 155706.
- (39) Ravindra, N. M.; Weeks, R. A.; Kinser, D. L. Optical properties of GeO<sub>2</sub>. *Phys. Rev. B: Condens. Matter Mater. Phys.* **1987**, *36*, 6132.
- (40) Xu, M.-F.; Shi, X.-B.; Jin, Z.-M.; Zu, F.-S.; Liu, Y.; Zhang, L.; Wang, Z.-K.; Liao, L.-S. Aqueous solution-processed GeO<sub>2</sub> an anode interfacial layer for high performance and air-stable organic solar cells. *ACS Appl. Mater. Interfaces* **2013**, *5*, 10866–10873.
- (41) Dalui, A.; Thupakula, U.; Khan, A. H.; Ghosh, T.; Satpati, B.; Acharya, S. Mechanism of versatile catalytic activities of quaternary CuZnFeS nanocrystals designed by a rapid synthesis route. *Small* **2015**, *11*, 1829–1839.
- (42) He, W.; Kim, H. K.; Wamer, W. G.; Melka, D.; Callahan, J. H.; Yin, J. J. Photogenerated charge carriers and reactive oxygen species in ZnO/Au hybrid nanostructures with enhanced photocatalytic and antibacterial activity. *J. Am. Chem. Soc.* **2014**, *136*, 750–757.
- (43) Mills, A.; Wang, J. Photobleaching of methylene blue sensitised by TiO<sub>2</sub>: An ambiguous system? *J. Photochem. Photobiol., A* **1999**, *127*, 123–134.
- (44) Mahmoud, M. A.; Saira, F.; El-Sayed, M. A. Experimental evidence for the nanocage effect in catalysis with hollow nanoparticles. *Nano Lett.* **2010**, *10*, 3764–3769.
- (45) Kumar, S.; Surendar, T.; Baruah, A.; Shanker, V. Synthesis of a novel and stable g-C<sub>3</sub>N<sub>4</sub>-Ag<sub>3</sub>PO<sub>4</sub> hybrid nanocomposite photo-

catalyst and study of the photocatalytic activity under visible light irradiation. *J. Mater. Chem. A* **2013**, *1*, 5333–5340.

(46) Chen, Z.; Zhang, N.; Xu, Y. J. Synthesis of graphene–ZnO nanorod nanocomposites with improved photoactivity and anti-photocorrosion. *CrystEngComm* **2013**, *15*, 3022–3030.

(47) Yang, W.; Zhang, L.; Hu, Y.; Zhong, Y.; Wu, H. B.; Lou, X. W. Microwave assisted synthesis of porous Ag<sub>2</sub>S–Ag hybrid nanotubes with high visible light photocatalytic activity. *Angew. Chem., Int. Ed.* **2012**, *51*, 11501–11504.

(48) Ju, Y.; Yang, S.; Ding, Y.; Sun, C.; Zhang, A.; Wang, L. Microwave-assisted rapid photocatalytic degradation of malachite green in TiO<sub>2</sub> suspensions: mechanism and pathways. *J. Phys. Chem. A* **2008**, *112*, 11172–11177.

(49) Chen, C. C.; Lu, C. S.; Chung, Y. C.; Jan, J. L. UV Light induced photodegradation of malachite green on TiO<sub>2</sub> nanoparticles. *J. Hazard. Mater.* **2007**, *141*, 520–528.

(50) Gaudette, N. F.; Lodge, J. W. Determination of methylene blue and leucomethylene blue in male and female fischer 344 rat urine and b6c3f1 mouse urine. *J. Anal. Toxicol.* **2005**, *29*, 28–33.

(51) Izadifard, M.; Langford, C. H.; Achari, G. Photocatalytic dechlorination of polychlorinated biphenyls using leuco-methylene blue sensitization, broad spectrum visible lamps, or light emitting diodes. *Environ. Sci. Technol.* **2010**, *44*, 9075–9079.

(52) Hallock, A. J.; Berman, E. S.; Zare, R. N. Ultratrace kinetic measurements of the reduction of methylene blue. *J. Am. Chem. Soc.* **2003**, *125*, 1158–1159.